ACS OMEGA

http://pubs.acs.org/journal/acsodf

Article

Capillary-Driven Boiling Heat Transfer on Superwetting Microgrooves

Yimin Li, Xiaolong Yang,* Xu Tian, and Yu Tang

Cite This: *ACS Omega* 2022, 7, 35339−35350

Read Online

ACCESS | Metrics & More | Article Recommendations | Supporting Information

ABSTRACT: Boiling can transfer a vast amount of heat and thereby is widely used for cooling advanced systems with high power density. However, the capillary force of most existing wicks is insufficient to surpass the liquid replenishing resistance for high-efficient boiling. Herein, we report a new microgroove wick on high-conductive copper substrates that was constructed via ultraviolet nanosecond pulsed laser milling. The phase explosion, combined with melting and resolidification effects of laser milling induces dense microcavities with sizes around several micrometers on the microgroove surface. The hierarchical microstructures significantly improve the wettability of the microgroove wicks to obtain strong capillary and meanwhile provide abundant effective nucleation sites. The boiling heat transfer in a visualized flat heat pipe shows that the new wicks enable sustainable liquid replenishing even under antigravity conditions, thus resulting in maximum 33-fold improvement of equivalent thermal conductivity when compared with the copper base. This research provides both scientific and technical bases for the design and manufacture of high-performance phase change cooling devices.

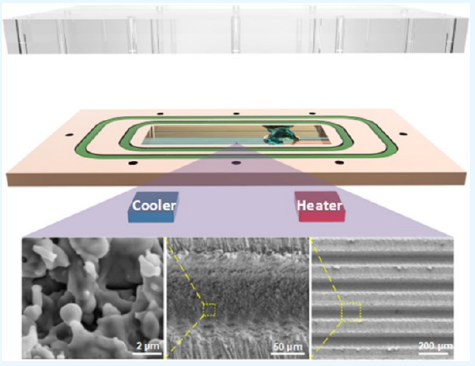

1. INTRODUCTION

Nowadays, most civilized activities of human beings involve thermal management. Thermal generation, transmission, and storage play an important role in many frontier fields.[1] For new energy facilities, e.g., fuel cell stacks, further improvement of the power density and the future lightweighting design remain challenging due to the rising temperature of the bipolar plates.[2−5] In the electronic field, with the ever-increasing rate of data processing, the power density of electronics has risen. The failure rate of electronic systems thus increases exponentially with the increased temperature. Reports revealed that 55% failure is caused by the overheated core electronic components.[6−8] As a result, development of efficient and lightweight cooling devices that can rapidly dissipate heat from those systems with high power density is desired. High heat-conductive materials are good candidates for this purpose. For example, aluminum and copper are most used materials for dissipating heat via conduction. However, those traditional materials are unable to extract the ever-increasing heat flux due to the relatively low thermal conductivity. Therefore, new promising materials, such as diamond, graphene, silicon carbide, and newly discovered BaS with extremely high thermal conductivity, are attracting intensive attentions. But heat dissipation capacity simply via the heat conduction is limited and the compatibility issues of the materials induced by direct contact between the heat-conductive materials and target components need careful consideration.[9,10]

Alternately, phase change heat transfer, e.g., boiling heat transfer, can extract a large amount of heat due to the high latent heat of the vapor;[11] particularly, when materials with heterogeneous thermal conductivities were used, an ultrahigh heat transfer limit can be reached.[12] The capillary-driven boiling heat transfer utilizes the inherent capillary force from the microstructures, commonly known as wicks, to transport the working fluid to the hot spot for phase change and thereby taking away the latent heat. The heat transfer of boiling reaches the limit, resulting in dry out at the hot spot, when the capillary force cannot surpass the resistance imposed by the viscous loss of liquid replenishing and pressure drop from vapor extraction. To improve the capillary force of the wicks, diverse microstructures, including grooves,[13] sintered powder/fibers,[14] mesh,[15] and composite structures[16,17] have been developed. Nevertheless, the capillary of those wicks is still far insufficient for liquid replenishing from a distance larger than 10 mm.[18] In addition, how to increase the effective nucleation sites for boiling while maintaining the strong capillary is vital and remains unclear.

Herein, we report a new microgroove wick on high-conductive copper substrates that were constructed via laser milling (Figure 1a). The phase explosion, combined with melting and resolidification effects of the ultraviolet nanosecond pulsed laser induces dense microcavities with sizes around

Received: August 22, 2022
Accepted: September 14, 2022
Published: September 26, 2022

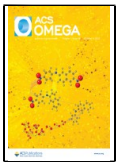

https://doi.org/10.1021/acsomega.2c05381
ACS Omega 2022, 7, 35339−35350

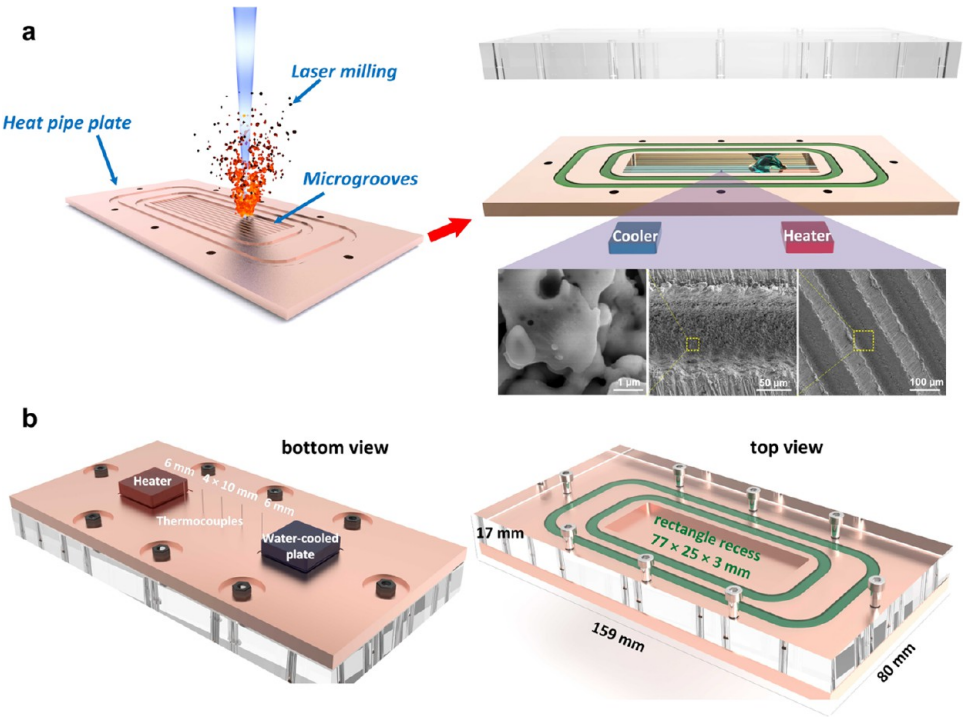

Figure 1. Schematic of the visualized flat heat pipe: (a) heat pipe assembly and wick fabrication and (b) diagram of the flat heat pipe structure.

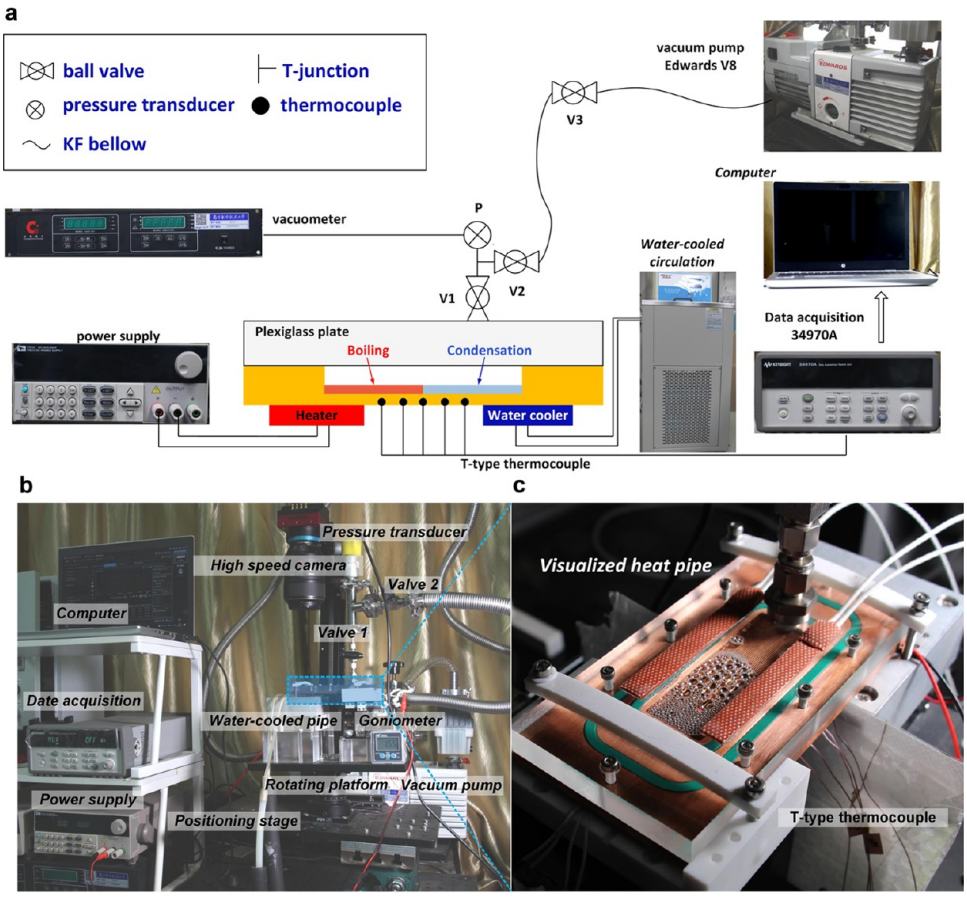

Figure 2. Visualized heat pipe test system: (a) schematic and (b) digital photo of the visualized heat pipe system and (c) digital photo of the visualized heat pipe assembly.

several micrometers on the microgroove surface. The hierarchical microstructures significantly improve the wettability of the microgroove wicks to obtain strong capillary and meanwhile provide abundant effective nucleation sites. The

https://doi.org/10.1021/acsomega.2c05381
ACS Omega 2022, 7, 35339−35350

boiling heat transfer test implemented on a visualized flat heat pipe (Figure 1b) shows that the new wicks enable sustainable liquid replenishing from a distance more than 70 mm even under antigravity conditions. The equivalent thermal conductivity of the hierarchical microgroove-wicked flat heat pipe demonstrates maximum 33-fold improvement compared with the copper base. This research provides both scientific and technical bases for the design and manufacture of high-performance phase change cooling devices.

2. EXPERIMENTAL SECTION

2.1. Fabrication of Microgroove Wicks. A copper base was immersed in acetic acid for 1 min to remove the surface oxide and contaminants[19] before subjected to laser milling using an ultraviolet nanosecond laser machining system (KY-M-UV3L, Wuhan Keyi). Scanning interval of 1 μm, scanning speed of 1500 mm·s^{-1}, and average output power of 3.3 W were held constant during the laser treatment (Figure S1). Microgrooves with widths of 100 ± 4, 203 ± 5, 303 ± 7 and 404 ± 13 μm were obtained by controlling the scanning path in a strip region. The microgroove ridge was set equal to the width for all samples.

2.2. Capillary Test. The capillary test was implemented on an assembled platform which consists of a high-speed camera, *XYZ*-axial stage, liquid pool, and light source (Figure S2). The sample for the capillary test was prepared by milling microgrooves in a region of 6 mm × 30 mm on a copper sheet (60 mm × 20 mm × 2 mm). The as-prepared sample was fixed on the *Z*-axial stage to move downward slowly to the liquid pool. The high-speed camera was used to record the liquid rising once the liquid contacted the microgrooves. The videos were then postprocessed to extract the frames so that the rising height at different times can be measured directly.

2.3. Assembly of Visualized Heat Pipe. The heat transfer performance of microgroove-wicked heat pipe is analyzed on a visualized heat pipe composed of a copper base and a plexiglass cover plate. The copper base with O-ring seal groove and rectangular recess (77 mm × 25 mm × 3 mm) was directly formed by NC machining (Figures S3 and S4). Microgroove wicks were textured in the bottom of the recess. Five holes with a diameter of 0.25 mm and a depth of 1.0 mm were drilled at the bottom of the copper base to bury the thermocouples (T-type, deviation 0.1 °C) for temperature acquisition. To evaluate the heat transfer performance of the heat pipe, a ceramic heater with adjustable heating power and a copper sink were installed at the evaporation and condensation sections, respectively, on the back of the heat pipe. The outlet of the thermostatic for the copper sink was 5 °C (high cooling power) and 20 °C (low cooling power), and the mass flow rate was 0.65 L·min^{-1}.

2.4. Test Platform for the Heat Pipe. As shown in Figure 2a, the visualized heat pipe test system mainly consists of a vacuum pump (Edwards, RV8), thermocouples, a pressure sensor, a data acquisition system (Keysight 34970A with 34901A module), a high-speed imaging system, and auxiliary facilities such as valves and connectors, power supplies, laptops, and light sources. The visualized heat pipe was connected to the vacuum through three ball valves, a T-joint, and a KF bellows. One of the valves (valve 1) was screwed directly into the plexiglass cover to connect the heat pipe chamber, and valve 2 was connected to the T-joint near the pressure sensor (Figure 2b,c). Noncondensable gases significantly reduce the heat transfer capacity of visual heat pipes, so all valves and connections were used in a high vacuum to ensure the removal of noncondensing gases. The whole visualized heat pipe assembly was installed on a rotating platform that can be tilted to a specific angle (−90°−90°).

2.5. Charge of Working Fluid. The compatibility between the fluid and wick materials should be carefully considered when selecting the working fluid. Water is compatible with copper and has high latent heat and a wide operatable temperature range (30−200 °C). Therefore, water is a commonly used working medium for electronic heat dissipation equipment. The tilting angle of the visualized heat pipe assemble was fixed at 50° for the charge of working fluid. Deionized water was degassed in a commercial vacuum chamber for at least 30 min to remove the noncondensable gas and then was pumped into the heat pipe chamber through valve 1 using a needle. The visualized heat pipe was initially completely flooded to eliminate the noncondensable gas inside. Then, valve 1 was closed, and valve 2 was opened to extract excess water and air between valve 1 and the vacuum pump. When the pressure drops to about 5.0 Pa, valve 1 was opened to remove some water. After each removal, the remaining water was collected in the lower part of the visualized heat pipe, so that the filling ratio can be calculated by the ratio of the water level to the chamber height. Valves 1 and 2 should be opened frequently and alternately to ensure precise control of the filling ratio.

2.6. Data Deduction. The equivalent thermal conductivity λ_{eff} was used to characterize the performance of the heat pipe and was deduced as follows[20]

$$\lambda_{eff} = -Q_{in}dx/A_s dT \quad (1)$$

where Q_{in} is the input heating power that can be adjusted with a DC power supply, T is the surface temperature, A_S is the cross-sectional area of the heat pipe, and x is the coordinate of the heat transfer surface. The temperature gradient dT/dx can be obtained using the following equation

$$dT/dx = ((T_4 - T_1)/L_{14} + (T_5 - T_2)/L_{25})/2 \quad (2)$$

where L_{ij} represents the distance between thermocouples T_i and T_j (Figures S6−S21). Substituting eq 2 into eq 1, the corresponding equation for the equivalent thermal conductivity will be

$$\lambda_{eff} = Q_{in}/(2A_s(T_4 - T_1)/L_{14} + (T_5 - T_2)/L_{25}) \quad (3)$$

3. RESULTS AND DISCUSSION

3.1. Surface Property of the Laser-Milled Microgrooves. Physical effects of the nanosecond pulsed laser milling of metal materials include melting, evaporation, boiling, and phase explosion.[21] When the pulsed laser with sufficient energy density acts on the material, the material is heated rapidly, and the temperature reaches the melting point, boiling point, and critical temperature of the material in turn. The laser energy density is too high, and the heat deposition time is too short (less than 100 ns); as a result, the surface pressure of the material cannot be balanced; the material does not boil in time, and thus, the state of superheating is established. When the internal bubbles in the melting materials grow to a certain size and number, a severe phase transition explosion occurs. The explosion zone produces a mixture of steam and liquid/solid micro/nanoparticles.[22] Nanosecond pulsed laser energy follows the Gaussian distribution, and the laser energy density at the beam (x, y) can be expressed as[22]

https://doi.org/10.1021/acsomega.2c05381
ACS Omega 2022, 7, 35339−35350

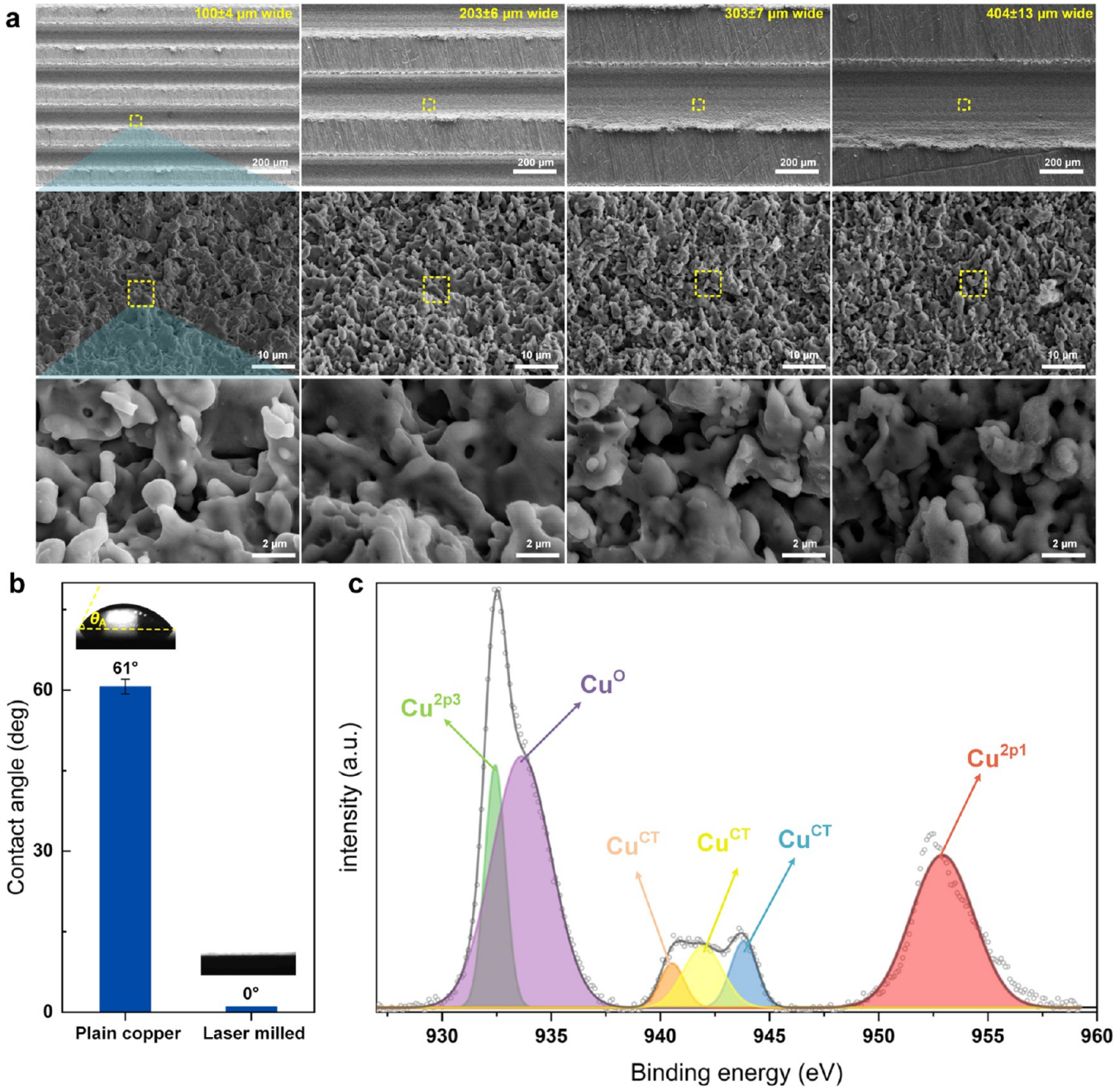

Figure 3. Surface property of laser-milled microgrooves: (a) SEM images of the microgrooves with different widths; (b) static contact angle of the plain copper and laser-milled copper; (c) XPS spectrum of laser-milled microgrooves.

$$I(x, y) = I_0 \exp\left(-2\left(\frac{\sqrt{(x - x_c)^2 + (y - y_c)^2}}{\omega_0}\right)^2\right) \quad (4)$$

where (x_c, y_c) is the central point coordinate of the spot and ω_0 is the waist radius of the laser beam ($\omega_0 = 10\ \mu m$). The peak energy density of the pulsed laser is[23]

$$I_0 = \frac{2E_p}{\pi\omega_0^2} = \frac{2P_a}{\pi\omega_0^2 f} \quad (5)$$

where E_p is the single pulse laser energy, P_a is the average output power of the pulse laser, and f is the laser repetition frequency. According to eq 5, the peak energy density of pulsed laser processing used in this work was calculated to 51.4 J·cm^{-2}. The threshold laser energy density that enables phase explosion for copper is 30 J·cm^{-2},[24] which manifests that the materials were removed mainly via phase explosion and evaporation from the center to the outside of the laser spot. By taking advantage of the laser-induced rapid material removal, microgrooves with designed width and depth can be shaped by controlling the scanning path and scanning cycles. It was notable that the cross-sectional profile of the microgrooves was inverted trapezoid due to the uniform Gaussian-like material removal at the laser milling region. Particularly, when the width of microgrooves is less than 100 μm, which is close to the waist radius of the laser beam, the cross-sectional profile of the laser-milled microgrooves is Gaussian-like V-shaped. The violent agitation of the melted

https://doi.org/10.1021/acsomega.2c05381
ACS Omega 2022, 7, 35339−35350

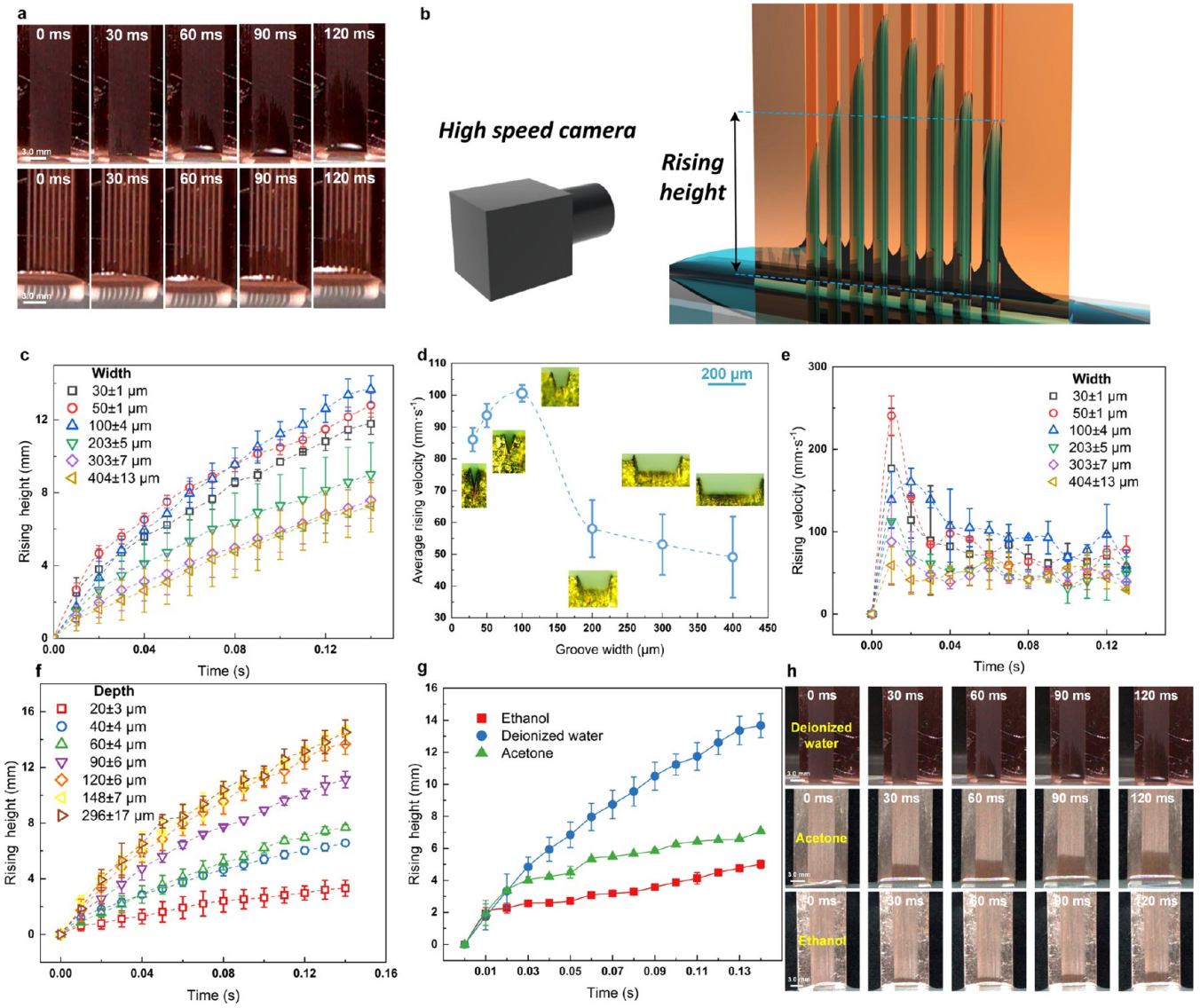

Figure 4. Capillary test on the microgroove wicks: (a) time-lapse images of capillary rising in the microgroove wicks with widths of 100 ± 4 μm (upper panel) and 404 ± 13 μm (lower panel); (b) schematic of the capillary rising test; (c) capillary rising height versus time for the microgrooves with different widths; (d) average capillary rising velocity versus microgroove width; (e) transient capillary rising velocity versus time for microgrooves with different widths; (f) capillary rising height versus time for microgrooves with different depths; (g) capillary rising height versus time for different liquids; (h) time-lapse images of capillary rising of different liquids in the microgroove wicks.

metals during phase explosion, together with the resolidification effect creates dense microcavities with the size of several micrometers (Figures 3a and S5). These unique hierarchical microgrooves significantly improve the surface superhydrophilicity (Figure 3b) and provide effective nucleation sites for boiling heat transfer.[25] XPS spectrum illustrates that copper atoms interact with oxygen atoms in the air under the action of laser, forming binding bonds (Figure 3c). It was evidenced that the copper oxide has no impact on the thermal conductivity of the copper base and is suitable for the heat transfer application.[26]

3.2. Capillary Transport. The capillary of the wicks is very important for enhanced phase change heat transfer as it determines the capacity of rewetting and liquid replenishing to the hot spot, thus dominates the heat transfer limit.[27,28] Microgroove wicks have strong capillary pressure and weak viscous resistance; in addition, the liquid replenishing direction can be easily manipulated for heat dissipation application on both 1-D and 2-D regions.

When the liquid wets the microgrooves, meniscus forms at the sidewall and bottom surface of the microgrooves with the aid of interfacial surface tension. Maximum dimension of the microgrooves is less than 400 μm, which is much smaller than the capillary length $l_{cp} = \sqrt{\gamma/(\rho g)}$, a function of surface tension γ, liquid density ρ, and gravity acceleration g (for deionized water, $l_{cp} \approx 2.7$ mm). This means that the surface tension governs the liquid interfacial shape, rather than the gravity, and it is reasonable to assume a perfect curve of the liquid meniscus in the microgrooves. The radius of the curvature of the liquid meniscus at the sidewall and bottom surface can thus be calculated by the following formula

$$r_{side} = \frac{\omega}{2\cos\theta_A}; \; r_{foot} = \frac{h}{\cos\theta_A} \tag{6}$$

where θ_A is the apparent contact angle of the inner surface of the microgrooves and ω and h are the width and depth of the

https://doi.org/10.1021/acsomega.2c05381
ACS Omega 2022, 7, 35339−35350

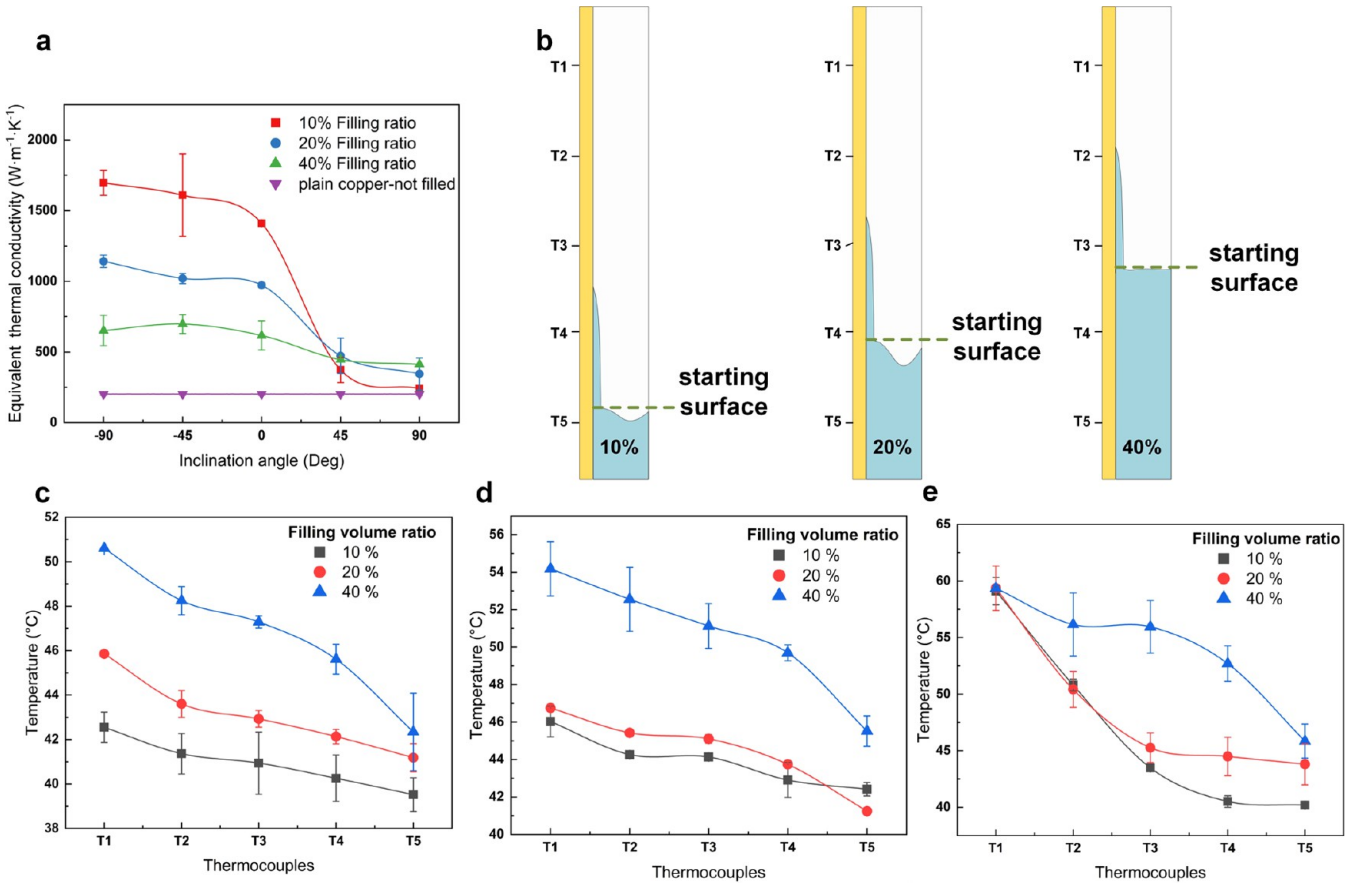

Figure 5. The influence of volume filling ratio and inclination angle on the heat transfer performance of the visualized flat heat pipe: (a) the equivalent thermal conductivity of the visualized flat heat pipes with different volume filling ratios at different inclination angles; (b) schematic of capillary wicking of the flat heat pipe with different volume filling ratios; temperature across the surface of the flat heat pipe with different volume filling ratios at inclination angles of (c) −90°, (d) 0°, and (e) 90°.

microgrooves, respectively. Ignoring the effects of hydrostatic pressure and air pressure, the Laplace pressure produced by the meniscus can be expressed as

$$\Delta p_{\mathrm{lap}} = \frac{\gamma}{r_{\mathrm{side}}} + \frac{\gamma}{r_{\mathrm{foot}}} = \frac{2\gamma \cos\theta_{\mathrm{A}}}{\omega} + \frac{\gamma \cos\theta_{\mathrm{A}}}{h} \tag{7}$$

while the hydraulic resistance is

$$R_{\mathrm{f}} = \frac{\eta u l}{A^2} \tag{8}$$

where η is the dimensionless geometrical correction factor, l is the capillary rising height, μ is the dynamic viscosity of the liquid, and $A = \int_{\Omega} \mathrm{d}_x \mathrm{d}_y$ is the cross-sectional area. The flow rate q_{m} can thereby be calculated using the following formula[27]

$$q_{\mathrm{m}} = \frac{\mathrm{d}l}{\mathrm{d}t}\omega h = \frac{\Delta p_{\mathrm{lap}}}{R_{\mathrm{f}}} \tag{9}$$

Finally, we can obtain an equation that describes the relationship between liquid transport distance and time by substituting eqs 7 and 8 into eq 9

$$\frac{dl}{dt}\omega h = \left(\frac{2\gamma \cos\theta_{\mathrm{A}}}{\omega} + \frac{\gamma \cos\theta_{\mathrm{A}}}{h}\right)\frac{A^2}{\eta u l} \tag{10}$$

According to the above analysis, the capillary driving pressure (Laplace pressure) increases with the decrease of the width of the microgrooves (Figure 4a−c), thus resulting in fast capillary rising in microgrooves with a small width. However, an interesting phenomenon is that the average capillary rising velocity V_{average} slows in the microgrooves with a width smaller than 100 μm (Figure 4d). This is possibly ascribed to the increased hydraulic resistance imposed on the V-shaped channels.[29] As shown in Figure 4e, we measured the transient capillary rising velocity $V_{\mathrm{transient}}$ ($V_{\mathrm{transient}} = (H_{\tau+5} - H_{\tau-5})/10$, where τ is the transient moment and H is the rising height at the corresponding time) and found that at the beginning of the capillary, the microgrooves with widths of 50 and 30 μm were faster than that with a width of 100 μm. But as the capillary rising proceeded, hydraulic resistance dominated and thus slowed the average capillary rising velocity.

The depth of the microgrooves determines both the Laplace pressure and hydraulic resistance thus is highly associated with the capillary wicking capability of a heat pipe. Substantial capillary rising experiments were implemented to analyze the impact of the microgroove depth on the capillary wicking capacity (Figure 4f). It is found that the rising velocity of the liquid initially creases with the depth but shows no obvious improvement when the depth of the microgroove is higher than 148 μm due to the shape deformation of the deep microgrooves. However, the transported liquid volume for 296 μm depth should be larger than that for 148 μm depth due to the increased cross-sectional area of the microgroove.

Different working fluids may be used in flat heat pipes under different working conditions. The capillary performance of those

https://doi.org/10.1021/acsomega.2c05381
ACS Omega 2022, 7, 35339−35350

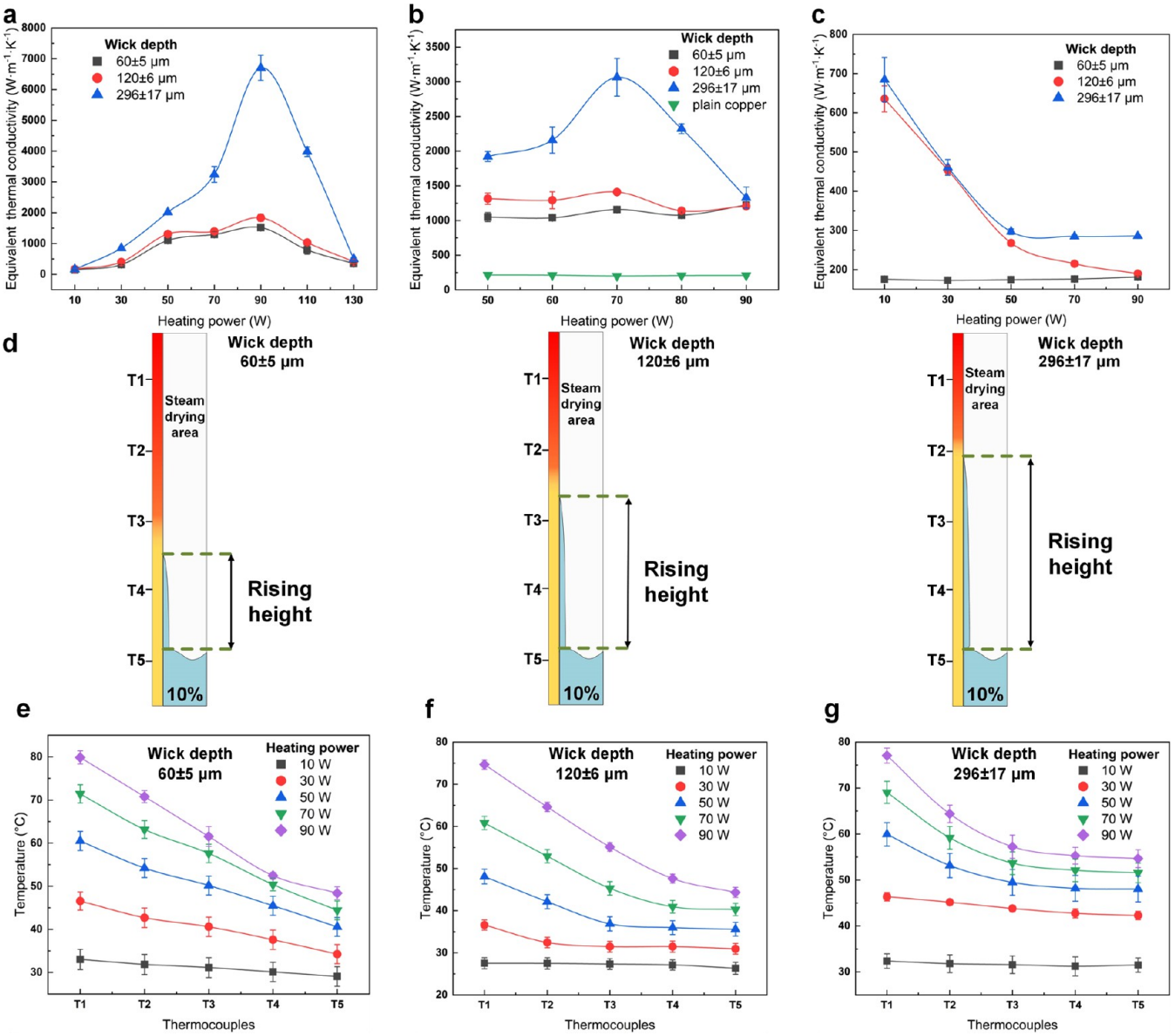

Figure 6. Heat transfer performance of microgroove wicks with different depths: the equivalent thermal conductivity of the heat pipes with different deep microgroove wicks at different input heating powers in the (a) along-gravity, (b) horizontal, and (c) antigravity working conditions; (d) schematic of the heat pipe with 60 ± 5, 120 ± 6, and 296 ± 17 μm deep microgroove wicks in the antigravity working condition; the temperature distribution at the bottom of the heat pipe with (e) 60 ± 5 μm, (f) 120 ± 6 μm, and (g) 296 ± 17 μm deep microgroove wicks in the antigravity working condition.

working fluids, which determines the heat transfer capacity, differs with the liquid properties, such as surface tension and viscosity. Herein, both ethanol and acetone were used to do the capillary rising test and to compare with the DI water results (Figure 4g). The capillary performance (the rising velocity) improves with the ratio of surface tension to the viscosity of the liquid (γ/μ) according to eq 10.

It is clear that γ/μ of DI water (γ/μ = 0.081) is much larger than that of ethanol (γ/μ = 0.020) and acetone (γ/μ = 0.072).[30] Thus, both the rising height and rising velocity of the DI water are higher than those of ethanol and acetone (Figure 4h).

According to eq 10, the capillary rising velocity also increases with the decrease of apparent contact angle θ_A of the groove surface. The microcavities produced by phase explosion and resolidification effects during nanosecond pulsed laser milling significantly improve the superhydrophilicity of the groove surface (static contact angle θ_A = 0°). As a result, the superhydrophilic surface combined with microgrooves design can achieve ultrafast capillary transport with an average velocity obviously higher than those of the traditional mesh and powder sintering structures.[13−17]

3.3. Boiling Heat Transfer Enhancement. The boiling heat transfer makes use of the latent heat of the phase transition of the working fluid to transfer a large amount of surface heat to ensure low surface temperature.[31] The form of boiling heat transfer changes from thin film evaporation to nucleate boiling and then to film boiling with the increase of superheat of the heated surface. Among them, nucleate boiling is the most effective. During nucleate boiling, nucleation, growth, and departure of bubbles occur alternately and constantly, taking away the surface heat. However, with the increase of temperature, the bubbles grow fast and join together to form

https://doi.org/10.1021/acsomega.2c05381
ACS Omega 2022, 7, 35339−35350

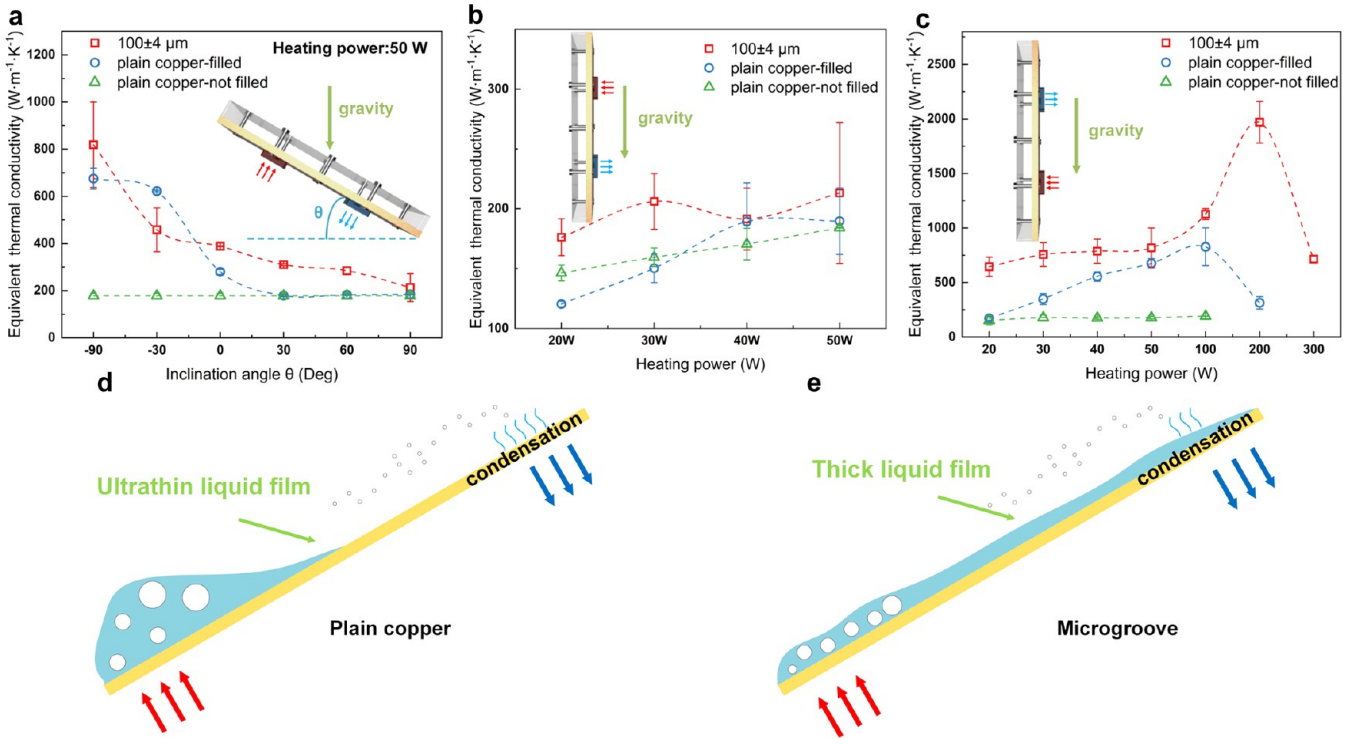

Figure 7. Heat transfer performance of the visualized flat heat pipe: (a) equivalent thermal conductivity of the visualized flat heat pipe orientated at different inclination angles at a heating power input of 50 W; equivalent thermal conductivity at different heating powers in (b) antigravity and (c) along-gravity working conditions; schematic of the liquid film detaining in the flat heat pipe (d) without wicks and (e) with microgroove wicks at an inclination angle of 30°.

an unstable vapor film, which leads to the surface drying out and the transition from nucleate boiling to film boiling. The surface heat transfer coefficient decreases significantly, and the surface temperature rises sharply until it burns out[32] (Movie S1). Thus, construction of microstructures with strong capillary that can overcome the bubble extraction pressure and viscous resistance to transport the working fluid to the hot spot for sustainable boiling was essential.

The heat transfer performance of the heat pipe can be evaluated by the equivalent thermal conductivity λ_{eff} obtained using eq 3. According to the equation, higher λ_{eff} represents more uniform surface temperature and better heat transfer performance.

The volume-filling ratio is readily important for a heat pipe; as a result, the dependence of the heat transfer performance on the volume-filling ratio should be first investigated and optimized. Additionally, the orientation of the heat pipe affects the capillary wicking performance of the wick structures, which is also highly associated with the volume-filling ratio. Therefore, the influence of the volume-filling ratio at different inclinations of the flat heat pipe on the heat transfer performance was analyzed.

As shown in Figure 5a, under the horizontal (inclination of 0°) and along-gravity (inclination of −90°) working conditions, the liquid volume-filling ratio of 10% allows for enough space for effective vapor exaction and meanwhile ensures sufficient capillary wicking to form a thin liquid film at the hot spot for sustainable evaporation; thus, the volume-filling ratio of 10% performs better. However, in the case of antigravity working conditions, the capillary wicking capability rather than the space for vapor exaction dominates the heat transfer performance of a heat pipe because the gravity hinders the capillary wicking of working fluid and early dry out normally occurs. The capillary wicking with a larger volume-filling ratio is better due to the small distance from the liquid level to the hot spot and weak gravity-imposed resistance (Figure 5b), which ensures an essential liquid film for evaporation on the hot spot and thus results in much more uniform temperature (Figure 5c−e). Therefore, the equivalent thermal conductivity of the heat pipe increases with the filling volume ratio.

Regarding the heat transfer performance of microgroove wicks with different depths, the equivalent thermal conductivity and the temperature distribution for wick depths of 60, 120, and 296 μm were analyzed at different inclination angles. It can be seen clearly that the wicks with 296 μm depth show the smallest temperature gradient and largest equivalent thermal conductivity among these three samples at a large-range heating power input and inclination angle due to a uniform liquid film for sustainable evaporation induced by strongest capillary wicking capability (Figure 6a−c). This capillary-induced change of the heat transfer performance is particularly significant in the antigravity working condition with high heating power input. For example, the temperature gradient for 120 μm depth rises obviously between the testing points T3 and T5 when the heating power input is higher than 70 W. This is possibly ascribed to that the capillary rising liquid volume in the shallow microgrooves was limited and insufficient for sustainable evaporation at a high thermal upload (Figure 6d−g). When the wick depth is further decreased to 60 μm, the capillary wicking weakens; thus, the temperature gradient exhibits the largest (Figure 6e).

To study the effect of cooling power on the performance of the heat pipe, the outlet of the thermostatic for the copper sink was varied from 20 °C (low cooling power) to 5 °C (high cooling power) and the mass flow rate was maintained constant

https://doi.org/10.1021/acsomega.2c05381
ACS Omega 2022, 7, 35339−35350

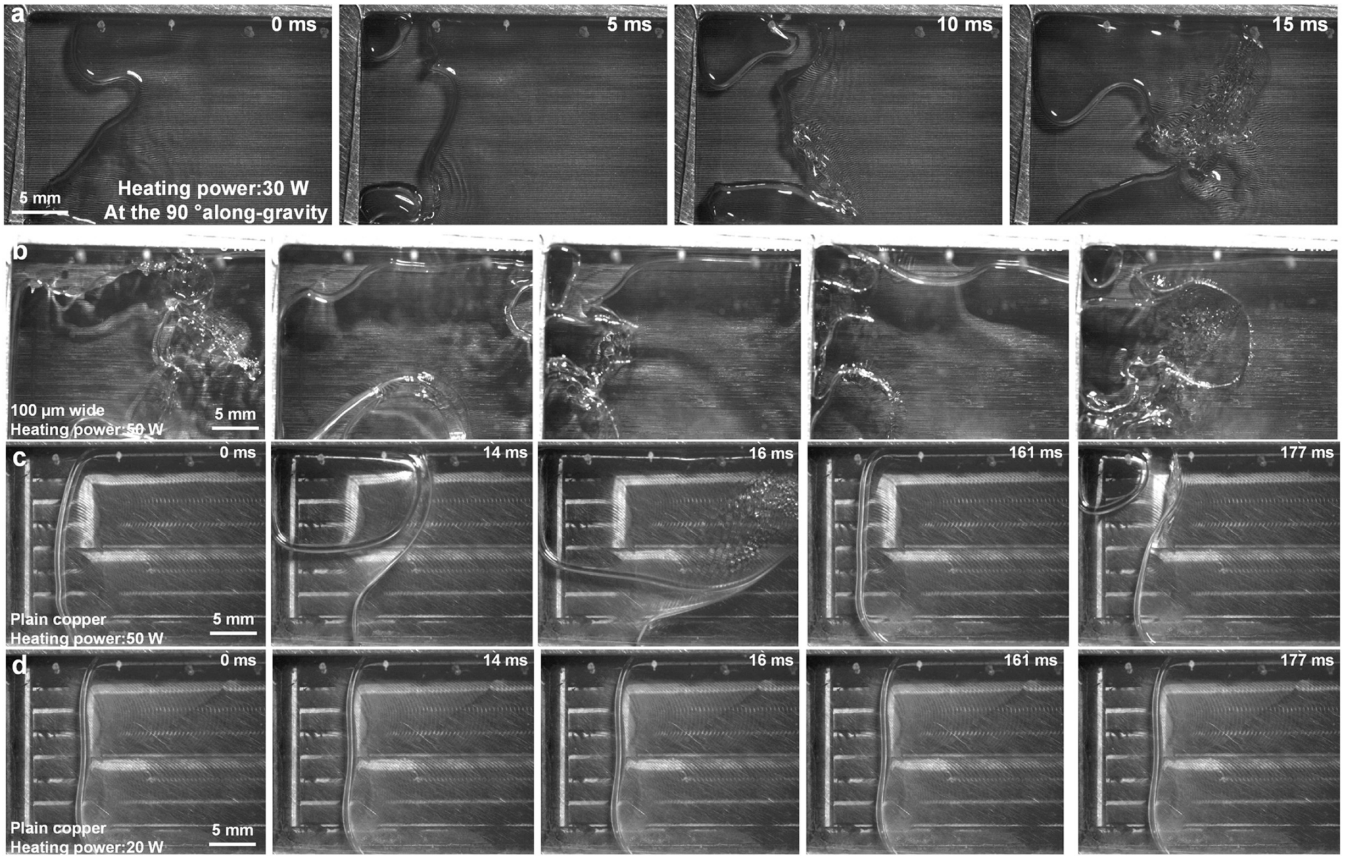

Figure 8. Time-lapse images of boiling in the visualized flat heat pipe in the along-gravity working condition: (a) boiling on the microgroove wicks with low cooling power at a heating power of 30 W; boiling on (b) the microgroove wicks and (c) plain copper at a heating power of 50 W with high cooling power; (d) visualization of the plain copper at a heating power of 20 W with high cooling power.

at 0.65 L·min^{-1}. For the high water-cooled power, the heat extraction rate at the condensation end increases, thus enlarging the maximum sustainable thermal uploads of the device but increasing the temperature gradient and decreasing the equivalent thermal conductivity (Figure 7).

At a much low heating power (20 W) and the along-gravity working condition, the microgroove-wicked flat heat pipe stars up due to the large amount of effective nucleation sites induced by phase explosion during laser milling, exhibiting a λ_{eff} of 644.8 W·m^{-1}·K^{-1}, which is 2.8-fold larger than the heat pipe without wicks. When the heating power increases, the capillary is the main limitation encountered in the working condition of the heat pipe. In addition to the dense nucleation sites, the laser-milled microgroove wicks were also endowed with strong capillary that enable the sufficient liquid replenishing at high heat flux. At the input heating power of 50 W, the equivalent thermal conductivity of the microgroove-wicked flat heat pipe that was orientated in the horizontal direction was 39% higher than that of the heat pipe without wicks (Figure 7a). It was notable that the strong capillary of the microgroove wicks can overcome the gravity and replenish the liquid to the hot spot for sustainable evaporation. The equivalent thermal conductivity of the microgroove-wicked flat heat pipe at a heating power of 30 W shows 37% higher than that without wicks in the antigravity working condition (Figure 7b).

In the along-gravity working condition, the advantage of strong capillary of the microgroove wicks is more predominant with the aid of gravity. The heat transfer performance of the microgroove-wicked flat heat pipe was much superior to that of plain copper, demonstrating a 10-fold improvement of equivalent thermal conductivity (Figure 7c). Moreover, the sustainable boiling can be maintained at an input heating power as high as 300 W.

However, when the inclination angle of the heat pipe was −30° (in the along-gravity working condition, the level of the evaporation end was lower than that of the condensation end), regarding the flat heat pipe without wicks (plain copper filled), the collected working fluid at the evaporation end and the detained ultrathin liquid film near the evaporation end can sustain the boiling/evaporation (see Movie S2). Meanwhile, the working fluid in the sample of "plain copper filled" will not be transported to the condensation end because of the absence of wicking force. As a result, the cold surface of the condensation end was exposed to the vapor, and condensation efficiency was much higher than the flat heat pipe with 100 μm wicks where the working fluid can be transported back to cover the cold surface of condensation, inhibiting the essential condensation (Figure 7d,e). In other words, in the along-gravity working condition with inclination of −30°, evaporation and condensation function normally for the flat heat pipe without wicks. Therefore, it is superior to the flat heat pipe with wicks.

On the contrary, when the flat heat pipe was oriented at an inclination of 30° (in the antigravity working condition, the level of the evaporation end was higher than that of the condensation end), the working fluid must be transported back to the evaporation end for sustainable phase change. The flat heat pipe with 100 μm wide microgroove wicks has strong capillary for

https://doi.org/10.1021/acsomega.2c05381
ACS Omega 2022, 7, 35339−35350

liquid replenishing to the evaporation end, and thus, its heat transfer performance is superior to that without wicks.

Regarding the low water-cooled power (the outlet temperature of the thermostatic for the copper sink was set at 20 °C), the heat extraction rate at the condensation end decreases, thus lowering the temperature gradient. High equivalent thermal conductivity can be obtained, but the maximum thermal uploads are weakened. The thermal uploads of the optimized wicks in the along-gravity, horizontal, and antigravity working conditions are 130, 90, and 90 W, respectively. The maximum obtained equivalent thermal conductivity in the horizontal working condition is 3064 W/mK for the wick depth of 300 μm, and the maximum data in the along-gravity working condition is 6704 W/mK, which is 2-fold higher than the horizontal condition and 33-fold higher than the plain copper without fluid charging.

Moreover, the thermal conductivity of the reported device can be increased further considering the following reasons: (1) the water-cooled heat sink was used to exact the heat from the condensation end of the flat heat pipe. This heat sink cooling power was not considered when calculating the equivalent thermal conductivity. Namely, only the heating power at the evaporation end was used as the Q_{in} in the Fourier's equation (eq 1) to calculate the equivalent thermal conductivity λ_{eff}; (2) to visualize the multiphase interface dynamics, a heterogeneous material (plexiglass cover) was attached on the copper plate to assemble the visualized system; as a result, the size of the heat pipe was technically enlarged for setting the O-ring seals and screwing. Provided that these sealing and fastening features can be omitted, the equivalent thermal conductivity of the heat pipe can reach 35755 W/mK (the cross-sectional area of the heat pipe A_S in eq 1 is downsized). Additionally, the visualized flat heat pipe was assembled by a wicked copper plate and a plexiglass cover with low thermal conductivity. Hence, the phase change process occurs only on one side of the device. Assuming that both sides of the heat pipe were textured by the optimized wicks, the equivalent thermal conductivity of the flat heat pipe can be increased further.

To characterize the boiling heat transfer performance of the microgroove wicks, we designed a visualized flat heat pipe with microgroove wicks and analyzed the bubble dynamics to reveal the heat transfer enhancement mechanism of the new wicks. We observed that the evaporation end of the heat pipe began to boil when the heating power reached 50 W under horizontal work (Movie S3) or reached 30 W in the 90° along-gravity working condition with the low cooling power (Figure 8a). With the high cooling power, it was visualized that the laser-milled microgroove wicks showed more intense bubble activities at a heating power of 50 W (Figure 8b), while the bubble growth frequency on the surface of plain copper was much lower (Figure 8c,d and Movie S4). On the other hand, the bubble ebullition occurred at many sites on the microgroove wicks, and the collision reaction between bubbles aggravated this reaction. This is because there are a large number of nucleation sites on the surface of microgrooves obtained by laser milling, and thus, bubbles can nucleate and grow at multiple sites, and the bubble ebullition period is short.[33−38] However, the plain copper lacks effective nucleation sites, bubbles are detected only at the corner, and the ebullition period is long.[39]

4. CONCLUSIONS

Microgroove wicks overlaid by dense microcavities with size around several micrometers were created on the high-conductive copper base using nanosecond pulsed laser milling. The microcavities induced by phase explosion and resolidification during the laser milling are effective nucleation sites for boiling and simultaneously improve the superhydrophilicity to obtain strong capillary.

The maximum thermal conductivity of the microgroove-wicked heat pipe in the horizontal working condition was 3064 W/mK for the wick depth of 296 μm, and the maximum data in the along-gravity working condition was 6704 W/mK, which is 2-fold higher than the horizontal condition and 33-fold higher than the plain copper without fluid charging.

The new microgroove wick on high-conductive copper substrates were constructed via laser milling that provided enlightenments on designing new heat transfer devices, for example, heat pipe to dissipate high flux heat from future integrated 5G microelectronic devices or fuel cells which usually have limited space for traditional cooling techniques.

■ ASSOCIATED CONTENT

Supporting Information

The Supporting Information is available free of charge at https://pubs.acs.org/doi/10.1021/acsomega.2c05381.

Boiling and drying out at 300 heating power input (MP4)

Comparison of boiling between plain copper and microgroove wicks with 50 W heating power input at the inclination of 30° (MP4)

Boiling in the visualized flat heat pipe (MP4)

Comparison of boiling between plain copper and microgroove wicks with 50 W heating power input in the along-gravity working condition (MP4)

Laser trajectory; capillary rise measurement system; drawing of the flat heat pipe; and temperature information across the bottom of the flat heat pipe (PDF)

■ AUTHOR INFORMATION

Corresponding Author

Xiaolong Yang − *College of Mechanical and Electrical Engineering, Nanjing University of Aeronautics and Astronautics, Nanjing 210016, P. R. China; Jiangsu Key Laboratory of Precision and Micro-Manufacturing Technology, Nanjing University of Aeronautics and Astronautics, Nanjing 210016, P. R. China; Aero-engine Thermal Environment and Structure Key Laboratory of Ministry of Industry and Information Technology, 210016 Nanjing, P. R. China;* orcid.org/0000-0002-2324-6172; Email: xlyang@nuaa.edu.cn

Authors

Yimin Li − *College of Mechanical and Electrical Engineering, Nanjing University of Aeronautics and Astronautics, Nanjing 210016, P. R. China; Jiangsu Key Laboratory of Precision and Micro-Manufacturing Technology, Nanjing University of Aeronautics and Astronautics, Nanjing 210016, P. R. China;* orcid.org/0000-0002-4527-8925

Xu Tian − *College of Mechanical and Electrical Engineering, Nanjing University of Aeronautics and Astronautics, Nanjing 210016, P. R. China; Jiangsu Key Laboratory of Precision and Micro-Manufacturing Technology, Nanjing University of Aeronautics and Astronautics, Nanjing 210016, P. R. China*

Yu Tang − *College of Mechanical and Electrical Engineering, Nanjing University of Aeronautics and Astronautics, Nanjing 210016, P. R. China; Jiangsu Key Laboratory of Precision and*

https://doi.org/10.1021/acsomega.2c05381
ACS Omega 2022, 7, 35339−35350

Micro-Manufacturing Technology, Nanjing University of Aeronautics and Astronautics, Nanjing 210016, P. R. China

Complete contact information is available at: https://pubs.acs.org/10.1021/acsomega.2c05381

Notes

The authors declare no competing financial interest.

■ ACKNOWLEDGMENTS

This research was financially supported by the National Natural Science Foundation of China (NSFC, 51905267), the Natural Science Foundation of Jiangsu Province (BK20192007, BK20190411), the China Postdoctoral Science Foundation (2020TQ0148), the Fundamental Research Funds for the Central Universities (NT2020011), and the opening foundation of Aero-Engine Thermal Environment and Structure Key Laboratory of Ministry of Industry and Information Technology of China (CEPE2020008).

■ REFERENCES

(1) Cho, H. J.; Preston, D. J.; Zhu, Y.; Wang, E. N. Nanoengineered materials for liquid−vapour phase-change heat transfer. *Nat. Rev. Mater.* **2017**, *2*, No. 16092.

(2) Yang, Y.; Li, W.; Xu, X.; Tong, G. Heat dissipation analysis of different flow path for parallel liquid cooling battery thermal management system. *Int. J. Energy Res.* **2020**, *44*, 5165−5176.

(3) Attinger, D.; Frankiewicz, C.; Betz, A. R.; Schutzius, T. M.; Ganguly, R.; Das, A.; Kim, C.-J.; Megaridis, C. M. Surface engineering for phase change heat transfer: A review. *MRS Energy Sustainability* **2014**, *1*, No. E4.

(4) Xu, X. M.; He, R. Review on the heat dissipation performance of battery pack with different structures and operation conditions. *Renewable Sustainable Energy Rev.* **2014**, *29*, 301−315.

(5) Zhang, J.; Zhang, L.; Sun, F.; Wang, Z. An Overview on Thermal Safety Issues of Lithium-ion Batteries for Electric Vehicle Application. *IEEE Access* **2018**, *6*, 23848−23863.

(6) Zhou, W.; Li, Y.; Chen, Z.; Deng, L.; Gan, Y. A novel ultra-thin flattened heat pipe with biporous spiral woven mesh wick for cooling electronic devices. *Energy Convers. Manage.* **2019**, *180*, 769−783.

(7) Khan, J.; Momin, S. A.; Mariatti, M. A review on advanced carbon-based thermal interface materials for electronic devices. *Carbon* **2020**, *168*, 65−112.

(8) Rehman, T.-u.; Ali, H. M. Experimental investigation on paraffin wax integrated with copper foam based heat sinks for electronic components thermal cooling. *Int. Commun. Heat Mass Transfer* **2018**, *98*, 155−162.

(9) Mudawar, I. Recent Advances in High-Flux, Two-Phase Thermal Management. *J. Therm. Sci. Eng. Appl.* **2013**, *5*, No. 021012.

(10) He, Y.; Sun, H. Mechanical strength and band alignment of BAs/GaN heterojunction polar interfaces: A first-principles calculation study. *Phys. Rev. Mater.* **2022**, *6*, No. 034603.

(11) Cheng, L.; Xia, G. Fundamental issues, mechanisms and models of flow boiling heat transfer in microscale channels. *Int. J. Heat Mass Transfer* **2017**, *108*, 97−127.

(12) Jiang, M.; Wang, Y.; Liu, F.; Du, H.; Li, Y.; Zhang, H.; To, S.; Wang, S.; Pan, C.; Yu, J.; et al. Inhibiting the Leidenfrost effect above 1,000 degrees C for sustained thermal cooling. *Nature* **2022**, *601*, 568−572.

(13) Ding, C.; Soni, G.; Bozorgi, P.; Piorek, B. D.; Meinhart, C. D.; MacDonald, N. C. A Flat Heat Pipe Architecture Based on Nanostructured Titania. *J. Microelectromech. Syst.* **2010**, *19*, 878−884.

(14) Maneemuang, S.; Kammuang-Lue, N.; Terdtoon, P.; Sakulchangsatjatai, P. Effect of pipe flattening on pressure drop in vapor core and thermal characteristic of miniature round and flat-shape heat pipe with sintered fiber wick. *Int. J. Heat Mass Transfer* **2021**, *176*, No. 121416.

(15) Wen, R.; Xu, S.; Lee, Y.-C.; Yang, R. Capillary-driven liquid film boiling heat transfer on hybrid mesh wicking structures. *Nano Energy* **2018**, *51*, 373−382.

(16) Tang, Y.; Deng, D.; Huang, G.; Wan, Z.; Lu, L. Effect of fabrication parameters on capillary performance of composite wicks for two-phase heat transfer devices. *Energy Convers. Manage.* **2013**, *66*, 66−76.

(17) Deng, D.; Tang, Y.; Huang, G.; Lu, L.; Yuan, D. Characterization of capillary performance of composite wicks for two-phase heat transfer devices. *Int. J. Heat Mass Transfer* **2013**, *56*, 283−293.

(18) Zhang, C.; Palko, J. W.; Barako, M. T.; Asheghi, M.; Santiago, J. G.; Goodson, K. E. Enhanced Capillary-Fed Boiling in Copper Inverse Opals via Template Sintering. *Adv. Funct. Mater.* **2018**, *28*, No. 1803689.

(19) Chavez, K. L.; Hess, D. W. A Novel Method of Etching Copper Oxide Using Acetic Acid. *J. Electrochem. Soc.* **2001**, *148*, G640.

(20) Li, J.; Lv, L.; Zhou, G.; Li, X. Mechanism of a microscale flat plate heat pipe with extremely high nominal thermal conductivity for cooling high-end smartphone chips. *Energy Convers. Manage.* **2019**, *201*, No. 112202.

(21) Dabby, F.; Un-Chul, P. High-intensity laser-induced vaporization and explosion of solid material. *IEEE J. Quantum Electron.* **1972**, *8*, 106−111.

(22) Qiao, Y.; Wang, X.; Qi, H.; Xu, H. Numerical simulation and parameters estimation of the time fractional dual-phase-lag heat conduction in femtosecond laser heating. *Int. Commun. Heat Mass Transfer* **2021**, *125*, No. 105355.

(23) He, H.; Wang, C.; Zhang, X.; Ning, X.; Sun, L. Facile fabrication of multi-scale microgroove textures on Ti-based surface by coupling the re-solidification bulges derived from nanosecond laser irradiation. *Surf. Coat. Technol.* **2020**, *386*, No. 125460.

(24) Cao, Y.; Shin, Y. C. Multi-scale modeling of phase explosion in high fluence nanosecond laser ablation and clarification of ablation depth prediction criterion. *Appl. Surf. Sci.* **2015**, *357*, 74−85.

(25) Wen, R.; Li, Q.; Wang, W.; Latour, B.; Li, C. H.; Li, C.; Lee, Y.-C.; Yang, R. Enhanced bubble nucleation and liquid rewetting for highly efficient boiling heat transfer on two-level hierarchical surfaces with patterned copper nanowire arrays. *Nano Energy* **2017**, *38*, 59−65.

(26) Tang, Y.; Yang, X.; Li, Y.; Lu, Y.; Zhu, D. Robust Micro-Nanostructured Superhydrophobic Surfaces for Long-Term Dropwise Condensation. *Nano Lett.* **2021**, *21*, 9824−9833.

(27) Hamidnia, M.; Luo, Y.; Li, Z.; Wang, X. Capillary and thermal performance enhancement of rectangular grooved micro heat pipe with micro pillars. *Int. J. Heat Mass Transfer* **2020**, *153*, No. 119581.

(28) Niu, J.; Xie, N.; Gao, X.; Fang, Y.; Zhang, Z. Capillary performance analysis of copper powder-fiber composite wick for ultra-thin heat pipe. *Heat Mass Transfer.* **2021**, *57*, 949−960.

(29) Mortensen, N. A.; Okkels, F.; Bruus, H. Reexamination of Hagen-Poiseuille flow: shape dependence of the hydraulic resistance in microchannels. *Phys. Rev. E.* **2005**, *71*, No. 057301.

(30) Tian, J.-M.; Chen, B. Dynamic behavior of non-evaporative droplet impact on a solid surface: Comparative study of R113, water, ethanol and acetone. *Exp. Therm Fluid Sci.* **2019**, *105*, 153−164.

(31) Kim, D. E.; Yu, D. I.; Jerng, D. W.; Kim, M. H.; Ahn, H. S. Review of boiling heat transfer enhancement on micro/nanostructured surfaces. *Exp. Therm. Fluid Sci.* **2015**, *66*, 173−196.

(32) Liang, G.; Mudawar, I. Pool boiling critical heat flux (CHF) − Part 2: Assessment of models and correlations. *Int. J. Heat Mass Transfer* **2018**, *117*, 1368−1383.

(33) Sharma, D.; Ghosh, D. P.; Saha, S. K.; Raj, R. Thermohydraulic characterization of flow boiling in a nanostructured microchannel heat sink with vapor venting manifold. *Int. J. Heat Mass Transfer* **2019**, *130*, 1249−1259.

(34) Shi, B.; Wang, Y.-B.; Chen, K. Pool boiling heat transfer enhancement with copper nanowire arrays. *Appl. Therm. Eng.* **2015**, *75*, 115−121.

(35) Pandelidis, D.; Anisimov, S. Numerical study and optimization of the cross-flow Maisotsenko cycle indirect evaporative air cooler. *Int. J. Heat Mass Transfer* **2016**, *103*, 1029−1041.

(36) Dedov, A. V. A Review of Modern Methods for Enhancing Nucleate Boiling Heat Transfer. *Therm. Eng.* **2019**, *66*, 881−915.
(37) Chen, J.; Ahmad, S.; Cai, J.; Liu, H.; Lau, K. T.; Zhao, J. Latest progress on nanotechnology aided boiling heat transfer enhancement: A review. *Energy* **2021**, *215*, No. 119114.
(38) Saneie, N.; Kulkarni, V.; Treska, B.; Fezzaa, K.; Patankar, N.; Anand, S. Microbubble dynamics and heat transfer in boiling droplets. *Int. J. Heat Mass Transfer* **2021**, *176*, No. 121413.
(39) Adam, A.; Han, D.; He, W.; Amidpour, M. Analysis of indirect evaporative cooler performance under various heat and mass exchanger dimensions and flow parameters. *Int. J. Heat Mass Transfer* **2021**, *176*, No. 121299.

https://doi.org/10.1021/acsomega.2c05381
ACS Omega 2022, 7, 35339−35350